POLITECNICO DI TORINO
Repository ISTITUZIONALE

Fracture Mechanics Characterization of an AnisotropicGeomaterial

(Article begins on next page)

14 May 2024

Fracture Mechanics Characterization of an Anisotropic Geomaterial

F. Barpi[1], S. Valente[1], M. Cravero[2], G. Iabichino[2], C. Fidelibus[2]

1   Department of Structural and Geotechical Engineering, Politecnico di Torino

2   Institute of Environmental Geology and Geoengineering, National Research Council of Italy, Torino

Nomenclature

- a_0: specimen notch depth

- a_{ij}: compliance coefficients

- α: softening law parameter

- b_0: notch width

- c_i: generic coefficients

- CMOD: crack mouth opening displacement

- D: core diameter

- $E_1 = E_2, E_3$: elasticity moduli transversely isotropic material

- η: deflection

- f_t: ultimate tensile strength

- $f_{t\perp\mathrm{s}}$: normal-to-bedding tensile strength

- $f_{t\|\mathrm{s}}$: parallel-to-bedding tensile strength

- $G_{13} = G_{23}$: shear moduli

- $G_{\mathrm{f}\|\mathrm{s}}$: fracture energy parallel-to-bedding plane

- H: semi-circular specimen height

- K_I: stress intensity factor

- K_Ic: critical value of stress intensity factor

- L: support span

- $\nu_{12}, \nu_{13} = \nu_{23}$: Poisson coefficients

- P: applied load

- r, θ: polar coordinates

- R: normal stress ratio

- s_j: roots of the characteristic equation

- S: specimen thickness

- $\boldsymbol{\sigma}$: stress tensor

- σ_θ: circumferential stress

- $\sigma_{\theta,\mathrm{m}}$: admissible maximum value of the circumferential tensile stress

- σ_n: normal stress in the cohesive law

- $\sigma_{n\mathrm{s}}$: normal stress on the bedding plane

- u_1, u_2, u_3: displacement components

- w_m: critical value of w_n

- w_n: normal-to-crack displacement discontinuity component

- $w_{\mathrm{m}\|\mathrm{s}}$: critical value of w_n for a crack opening parallel to bedding

- $w_{\mathrm{t}1}, w_{\mathrm{t}2}$: displacement discontinuity tangential components

- W: semi-circular specimen weight

- x_1, x_2: crack local coordinate system

- x, y, z: Cartesian coordinates

1. Introduction

Argillites are considered worldwide as potential host rock for high level radioactive waste given the low permeability and strong adsorption potential. However, the excavation of the galleries of a repository would produce a disturbed zone around the boundaries rich of new fractures which may enhance the conductivity of the rock along the gallery axis. Several mine-by experiments have been performed in Underground Research Labs (URLs) to investigate the

3

features of such a disturbed zone. In Mont Terri URL (Kanton Jura, Switzerland) the EZ-B experiment was specifically conceived for the measurement of excavation-induced fractures around a small chamber ([1]).

The host rock of the URL is a particularly compact and resistant argillite, known as the Opalinus Clay (OPA). During experiments, boreholes were excavated and OPA samples were subjected to fracture mechanics tests at the rock mechanics lab lab of IGAG-CNR[1]. The tests aimed at the understanding of the fracturing process occurring in OPA at Mont Terri; the rock may be considered a transversely isotropic geomaterial, whose planes of isotropy coincide with the bedding.

In such a rock Fracture Mechanics (FM) parameters are orientation-dependent. Bedding planes in the samples are aligned 45° with respect to the borehole axis. Semi-Circular specimen under three-point Bending (SCB) FM tests were accomplished to derive these orientation-dependent parameters. The results were interpreted by resorting to a three-dimensional Cohesive Crack Model (CCM) in the framework of the Non-Linear Fracture Mechanics (NLFM) theory. The advantages of a NLFM model with respect to a Linear Elastic Fracture Mechanics (LEFM) model are the following: both pre-peak and post-peak (softening) phases can be simulated by means of CCM; the requirements in terms of minimum specimen size are less restrictive.

Mode-I tensile crack growth was addressed in these tests. Mode-I is in fact deemed as a dominant process around a tunnel, even at the sidewalls where the crack growth under compressive stress is driven also by tensile failure at the tips.

The note reports a synopsis of the results of the tests, together with the related interpretation via CCM, anticipated by a short review of the existing contributions about the crack growth in anisotropic materials and a description of the features of the CCM. A comparison is also given with the results of the

---

[1]Institute of Environmental Geology and Geoengineering, National Research Council of Italy, Torino, Italy

application of a LEFM model. Finally, scale-dependent effects are addressed and remarks on the importance of a careful petrographical analysis, aimed at the definition of type, extension and occurrence of heterogeneities, are also reported.

2. Crack growth in anisotropic materials

Scientific contributions concerning crack growth in Mode-I in anisotropic materials are framed into LEFM ([2], [3] and [4]).

The essential position underpinning LEFM is the lack of a plastic zone at the tip of a crack. This implies a fully elastic behavior with stress singularities. Rather than comparing the stresses with some reference values to indicate failure, the severity of the stress field around the crack tip is measured by a factor applied to the asymptotically singular solution. This factor is called Stress Intensity Factor (SIF). The value reached by SIF at the onset of crack growth can be assumed as a property of the materials and called critical value of the SIF. If the relative displacement of the crack walls is characterized by the opening component, then the corresponding SIF is called K_{I} and the critical value is called K_{Ic} (fracture toughness).

A solution for the stress field around sharp cracks (under tensile loading) in infinite anisotropic plane domain is available (see [5]) and described in the following.

With reference to a polar system of coordinates (r,θ) centered at the tip of a crack, the circumferential stress is as follows:

$$\sigma_\theta = \frac{K_{\mathrm{I}}}{\sqrt{2\pi r}} \mathrm{Re}\left[\frac{1}{s_1 - s_2}\left(s_1\left(s_2\sin\theta + \cos\theta\right)^{3/2} - s_2\left(s_1\sin\theta + \cos\theta\right)^{3/2}\right)\right] \quad (1)$$

for Mode-I loading and:

$$\sigma_\theta = \frac{K_{\mathrm{II}}}{\sqrt{2\pi r}} \mathrm{Re}\left[\frac{1}{s_1 - s_2}\left(\left(s_2\sin\theta + \cos\theta\right)^{3/2} - \left(s_1\sin\theta + \cos\theta\right)^{3/2}\right)\right] \quad (2)$$

for Mode-II. In Equations 1 and 2 s_j represents the complex roots of the following characteristic equation:

$$a_{11}s^4 - 2a_{16}s^3 + (2a_{12} + a_{66})s^2 - 2a_{26}s + a_{22} = 0 \qquad (3)$$

where a_{ij} are the compliance coefficients with reference to the coordinate system of the crack (x_1 aligned with the crack). In case the crack is aligned with one of the principal direction of anisotropy, the previous equation simplifies as follows:

$$a_{11}s^4 + (2a_{12} + a_{66})s^2 + a_{22} = 0 \qquad (4)$$

where the elastic compliance coefficients are related to the engineering constants: $a_{11} = 1/E_1$, $a_{22} = 1/E_2$, $a_{12} = a_{21} = -\nu_{12}/E_1$, $a_{66} = 1/G_{12}$.

By compounding Equations 1 and 2 one has:

$$\sigma_\theta = \frac{K_{\mathrm{I}}}{\sqrt{2\pi r}} \mathrm{Re}\left[c_1 \left(s_1 c_2 - s_2 c_3\right)\right] + \frac{K_{\mathrm{II}}}{\sqrt{2\pi r}} \mathrm{Re}\left[c_1 \left(c_2 - c_3\right)\right] \qquad (5)$$

where c_i coefficients are as follows:

$$
\begin{aligned}
c_1 &= \frac{1}{s_1 - s_2} \\
c_2 &= \left(s_2 \sin\theta + \cos\theta\right)^{3/2} \\
c_3 &= \left(s_1 \sin\theta + \cos\theta\right)^{3/2}
\end{aligned}
$$

The propagation criterion for the anisotropic case requires to maximize the following *normal stress ratio* R from crack tip:

$$R(r,\theta) = \frac{\sigma_\theta}{\sigma_{\theta,\mathrm{m}}} \qquad (6)$$

where $\sigma_{\theta,\mathrm{m}}$ represents the admissible maximum value of the circumferential tensile stress, which is a property of the material. This limit value can be defined from Equation 1. It is:

$$\sigma_{\theta,\mathrm{m}} = \frac{K_{\mathrm{Ic}}(\theta)}{\sqrt{2\pi r}} \qquad (7)$$

where the fracture toughness Mode-I K_{Ic} is orientation-dependent and has an elliptical variation as follows:

$$K_{\text{Ic}}(\theta) = K_{\text{Ic},1} \cos^2 \theta + K_{\text{Ic},2} \sin^2 \theta \tag{8}$$

By considering Equations 5, 7, 8, the normal stress ratio R is then equal to:

$$R(\theta) = \frac{K_{\text{I}}\text{Re}\left[c_1 \left(s_1 c_2 - s_2 c_3\right)\right] + K_{\text{II}}\text{Re}\left[c_1 \left(c_2 - c_3\right)\right]}{K_{\text{Ic},1} \cos^2 \theta + K_{\text{Ic},2} \sin^2 \theta} \tag{9}$$

Under a specific combination of loads, the crack propagates along the direction θ_0 for which R is 1. Equation 9 represents an important step towards the understanding of the processes involving cracking in anisotropic solids.
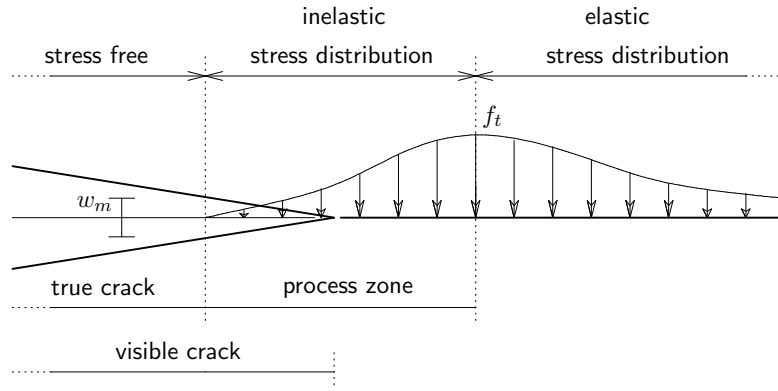
3. The cohesive crack model

Figure 1: Scheme of the Fracture Process Zone according to the Cohesive Crack Model

LEFM theories are adequate when the plastic zone at the tip of a crack is small compared to the crack length, as occurring for brittle bodies. On the contrary, experimental tests on specimens show that K_{Ic} for concrete, rock and masonry depends on size. These materials belong to a class called quasi-brittle materials, also known as concrete-like materials. This scale dependency is conceptually linked with the existence of a relatively large (with respect to the crack size) and non-linear zone in front of a crack tip. To overcome the limitations of LEFM, the cohesive crack model was introduced first by Barenblatt [6]

7

and Dugdale [7] and later applied to concrete by Hillerborg et al. [8], Bocca et al. [9, 10, 11], Bocca and Carpinteri [12] and Barpi and Valente [13].

According to this model when the principal tensile stress achieves the ultimate tensile strength f_t a complex non-linear behaviour occurs at the microscale. This behaviour can be simulated by assuming a fictitious crack extension where the material, albeit damaged, is still able to transfer stresses that are a decreasing function of displacement discontinuity component w_n, i.e., the relative normal displacement of the crack walls. Along the crack two distinct points are marked: the fictitious crack tip, where the non-linear phenomenon starts and real crack tip, where w_n achieves the critical value w_m. Beyond the last point no stress transfer occurs and the crack is stress free. The zone between the tips is called Fracture Process Zone (FPZ). The material response outside FPZ is considered linear. Figure 1 shows a scheme of FPZ.

4. Description of tests and results

In this section a description of the equipment utilized and type of test is given together with the illustration of the results obtained.

In order to define OPA FM parameters and given the intrinsic heterogeneity of such a material, there was the need to accomplish a sufficient number of tests in spite of a limited amount of material available, therefore the SCB test was selected. This test is an accurate and fast method to measure FM parameters when core-based cylindrical samples are available. The preparation time is short (provided the rock type is not sensitive to machining) and set up of the equipment is relatively easy. During the test a loading machine drives to failure a 5-cm-thick semi-circular specimen bending on two support rollers. The specimen is produced by cutting a slice from the core and then operating a further cut along a diameter to split the slice in two halves. Then a notch is machined from the center of the semi-circular specimen (see Figure 2). For water-sensitivity materials as OPA, cutting is generally performed dry with a cylindrical saw. Cutting of the slice along the diameter results probably in a loss of material,
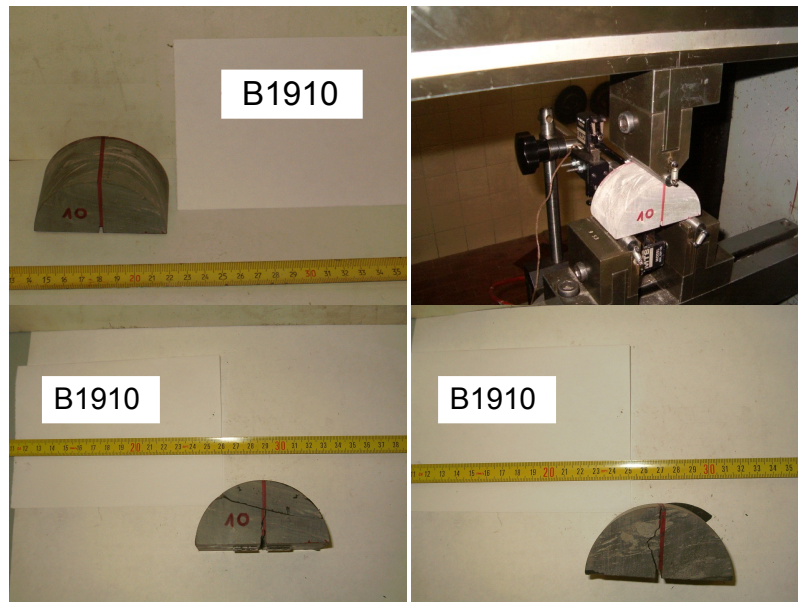
Figure 2: SCB test. A crack developed initially along the plane of the notch, then a further crack along weak bedding plane propagated giving rise to a multiple-crack failure

therefore the two halves may be not perfectly semi-circular. When required the basis of the half can be regularized.

Tests on the collected samples were performed in a hydraulic servo-controlled machine. With the increase of the applied load P a clip gauge extensometer measured the Crack Mouth Opening Displacement (CMOD) up to the specimen failure. CMOD is in practice the relative horizontal displacement measured at the mouth of the notch. Also the vertical displacement (deflection η) at the base of notch was monitored. Some of the tests were run at a constant deflection rate (0.4÷0.6μ/s), some at constant CMOD rate (0.03÷0.05μ/s).

As expected the ease to break along the bedding interfered strongly with the expected crack growth in many tests: cracks appeared to propagate initially along the plane of the notch and loading, then for the occurrence of weaker bedding planes they diverted giving rise sometimes to complex three-dimensional crack patterns.

S.	x	D	H	S	W	a_0	b_0
B0302	7.57-7.78	82.6	39.6	44.8	296.54	5.7	2.0
B1906	0.15-0.28	79.6	38.2	47.5	280.55	7.1	2.5
B1907	0.15-0.28	79.6	38.3	47.7	276.68	7.3	2.8
B1910	0.40-0.50	79.6	38.3	43.1	256.47	5.0	2.3
B1911	0.50-0.60	79.6	38.4	43.1	253.06	5.3	2.0
B1912	0.85-0.92	79.5	37.6	37.9	212.44	5.5	2.3
B1913	0.92-1.00	79.6	39.4	38.0	226.41	6.0	2.1
B1917	1.30-1.50	79.7	39.1	43.1	257.81	5.6	2.1
B1918	1.70-1.90	79.6	39.3	41.0	243.74	5.8	2.3

Table 1: List of the specimens. Legenda: x[m] distance from the top, D[mm] diameter of the core, H[mm] semi-circular specimen height, S[mm] thickness, W[g] semi-circular specimen weight, a_0[mm] notch depth, $b_0$notch width. The support span L[mm] is always 62 mm

A series of 23 specimens was tested, only in 9 the crack followed predominantly the plane of the notch, thus providing the response along that plane. In the remaining tests crack propagated initially along the plane of the notch but then diverted soon to follow a bedding plane. In these cases the load-versus-CMOD plot resulted meaningless and test was disregarded. Data of the 9 best specimens are reported in Table 1 while the results in terms of CMOD and deflection η (CMOD$_\mathrm{p}$ and η_p respectively) at peak load P_p are reported in Table 2. The values of η may be biased by initial settlement due to high strain occurring close to the support rollers. *The experimental results are presented in Figures 3 and 4 in terms of load against CMOD and load against deflection.*

The evaluation of fracture toughness K_Ic (Mode-I) was performed by the application of the following relation [14] that fits the results of FEM simulations by Chong et al. [15]:

$$K_\mathrm{Ic} = \frac{P_\mathrm{p}}{DS}\sqrt{\pi a_0}\left[4.47 + 7.4\frac{a_0}{D} - 106\left(\frac{a_0}{D}\right)^2 + 433.3\left(\frac{a_0}{D}\right)^3\right] \qquad (10)$$

In Table 3 the derived K_Ic values are reported for the selected specimens.

S.	P_{p}[N]	$\mathrm{CMOD_p}$[μm]	η_{p}[μm]
B0302	1600	23	370
B1906	1827	14	319
B1907	1400	48	228
B1910	1231	84	236
B1911	1314	15	244
B1912	1573	14	374
B1913	1428	44	272
B1917	1986	20	353
B1918	1069	47	195

Table 2: Results from the selected specimens: S. specimen, P_{p}, $\mathrm{CMOD_p}$, η_{p} load, CMOD and deflection at peak

S.	K_{Ic}
B0302	0.27
B1906	0.33
B1907	0.26
B1910	0.21
B1911	0.23
B1912	0.32
B1913	0.30
B1917	0.35
B1918	0.20

Table 3: $K_{\mathrm{Ic}}[\mathrm{MPa}\sqrt{\mathrm{m}}]$ for the selected specimens

Given the orientation of the bedding with respect to plane of the notch, these values refer to the Mode-I fracture toughness for cracks opening normal to the bedding, therefore, conforming with Equation 8, it is the principal maximum value $K_{\mathrm{Ic,1}}$. The mean value and standard deviation are respectively 0.27 and $0.05\mathrm{MPa}\sqrt{\mathrm{m}}$.
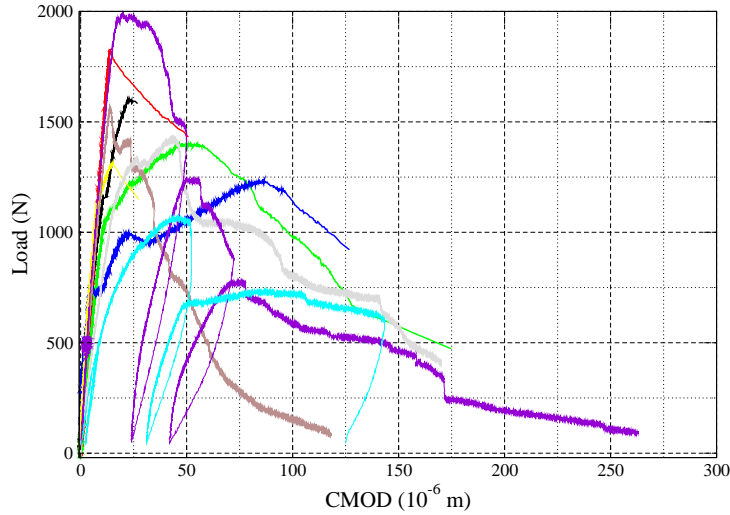
Figure 3: CMOD against load P for the selected 9 specimens

Rummel et al. [16] measured a $K_{Ic,1}$ value of 0.53 MPa$\sqrt{m}$ for OPA. They used three-point-bending tests with Chevron notched cores on borehole material and mini-plugs. The axial bending displacement rate was kept constant and equal to 1µ/s. The discrepancy between the results from Rummel et al. [16] and the results provided herein may depend on several factors, like specimen geometry and testing method [17] and scale (see the importance of the scale effect later on). OPA mechanical response is also strongly conditioned by the water content and loading rate. With reference to the last factor, Haberfield and Johnston [18] argued that a negative excess of pore-water pressure in the crack tip yield zone may occur during a FM test in soft rocks. For a relatively high loading rate and materials of low diffusivity this excess may not dissipate, thus a larger apparent fracture toughness may be measured. The SCB tests are performed at a lower rate than the three-point-bending tests of Rummel et al [16].
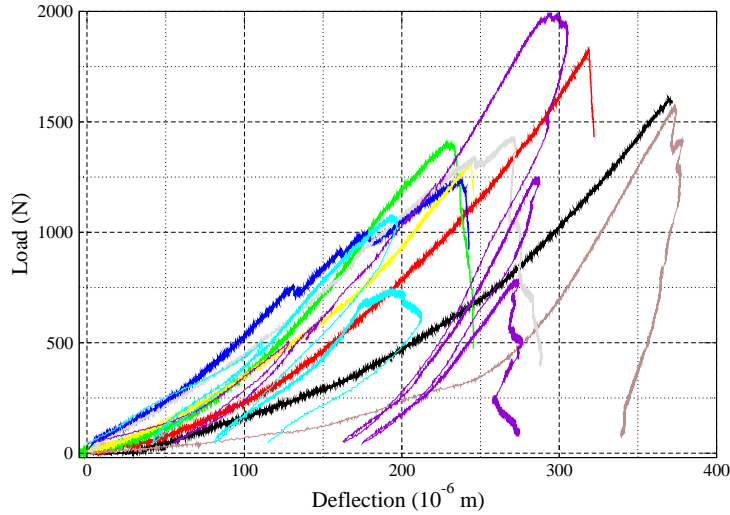
Figure 4: Deflection η against load P for the selected 9 specimens

5. Setup of NLFM numerical model

As previously mentioned, LEFM is a rather simple model for the interpretation of FM tests in geomaterials. In fact the assumption of a negligible plastic zone is generally not accepted for geomaterials. Furthermore, the fracture toughness as derived by Eq. 10 is based on the assumption of an isotropic medium, thus an error is introduced in the assessment. It is therefore suggested to perform the interpretation of the SCB tests by means of a three-dimensional numerical NLFM model, in which the anisotropy is explicitly included.

As far as the criterion for crack propagation is concerned, the details are in what follows. Given a fixed FEM mesh of a NLFM numerical model, the finite stress computed at a crack tip depends on the mesh itself. In particular, at a given applied load, the stress increases inversely to the mesh size, therefore there is a lack of mesh objectivity. However it is demonstrated that the initial (linear elastic) part of the P-CMOD curve does not depend on the mesh. It is assumed

13

herein that this phase finishes when the maximum principal stress (normal to the notch plane and paralell to bedding) achieves the parallel-to-bedding tensile strength $f_{t\|s}$.

Due to the symmetric boundary conditions of the specimen, the load-induced damage is localized along the notch plane. Within FPZ the residual stresses are called *cohesive stresses* and are decreasing functions of displacement discontinuity w_n. According to CCM the material outside FPZ behaves linearly, whereas the non-linear part of the model is confined within FPZ. With reference to Figure 1, in a three-dimensional model FPZ becomes a surface whereas the real crack tip and the fictitious crack tip become a line. Given the three-dimensionality of the model, the displacement discontinuity is characterized by the component w_n normal to the notch plane and two tangential components w_{t1} and w_{t2}. Due to the symmetry it results $w_{t1} = w_{t2} = 0$ and $\tau_1 = \tau_2 = 0$, where τ_1 and τ_2 are the tangential stress respectively parallel to w_{t1} and w_{t2}.

The damage process at FPZ is characterized by an uniaxial softening law (implemented in the commercial code ABAQUS [19]: $\sigma_n = \sigma_n(w_n)$, which is based on the exponential relation proposed by [20], specialized herein for anisotropic materials:

$$\frac{\sigma_n}{f_{t\|s}} = 1 - \frac{1 - e^{\frac{-\alpha\,w_n}{w_{m\|s}}}}{1 - e^{-\alpha}} \tag{11}$$

where $w_{m\|s}$ is the critical value for w_n for a crack normal to bedding (and opening displacement parallel to bedding). For $w_n > w_{m\|s}$ no stress transfer occurs and therefore the crack is stress-free.

The softening law is plotted in Figure 5 for α equal to 5 (a typical value for concrete-like materials). The area under this curve is the energy necessary to obtain a unit area of stress-free crack surface and corresponds to the *Mode-I fracture energy* $G_{f\|s}$.

For a transversely isotropic material the elastic properties of the material are axially-symmetric with respect to the axis normal to the bedding ([21]). Five constants are independent, elasticity moduli E_1 and E_3, Poisson coefficients
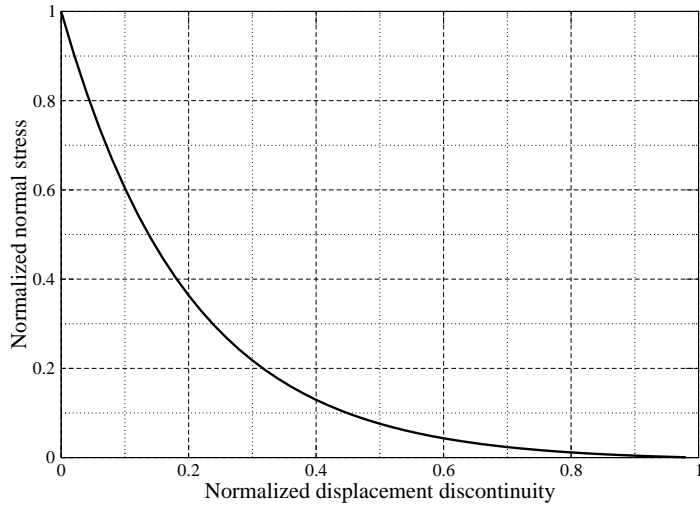
Figure 5: Softening law for α=5

$E_1 = E_2$	E_3	ν_{12}	$\nu_{13} = \nu_{23}$	$G_{13} = G_{23}$
GPa	GPa	-	-	GPa
10	4	0.33	0.24	1.2

Table 4: Elastic material properties.

ν_{12} and ν_{13} and shear modulus G_{13}, being axes 1 and 2 in the bedding plane. Table 4 reports the assumed values, that are recommended by [21] and allow a good fitting of the experimental results in the initial part of P-CMOD diagram.
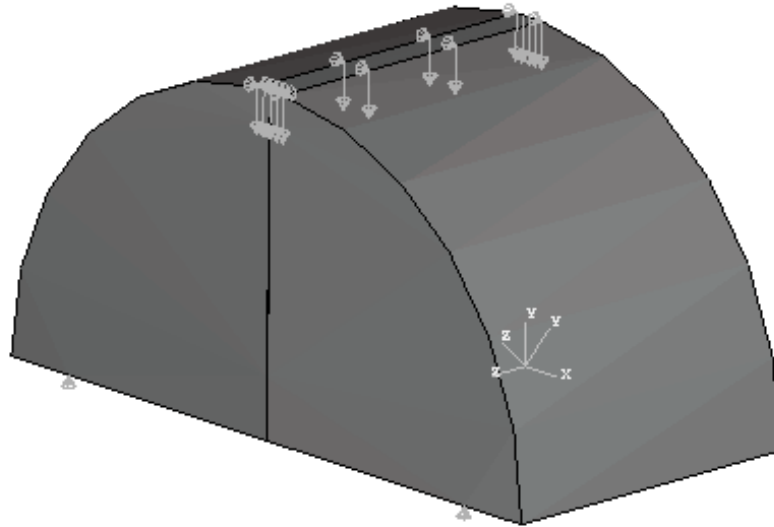
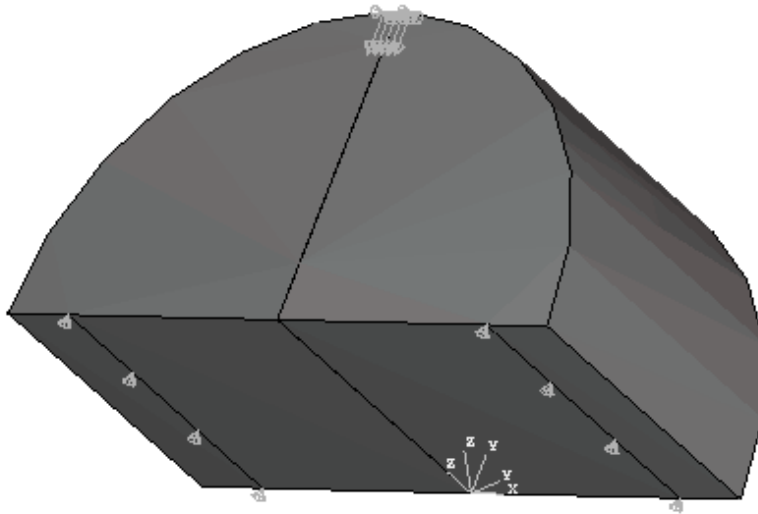Figure 6: Boundary conditions applied to the solid model

Figure 7: Boundary conditions applied to the solid model

Figures 6 and 7 show two axonometric views of the specimen model, respectively with indication of applied loads and boundary conditions from up and from below. The non-linear phenomena are localized along the two vertical sur-
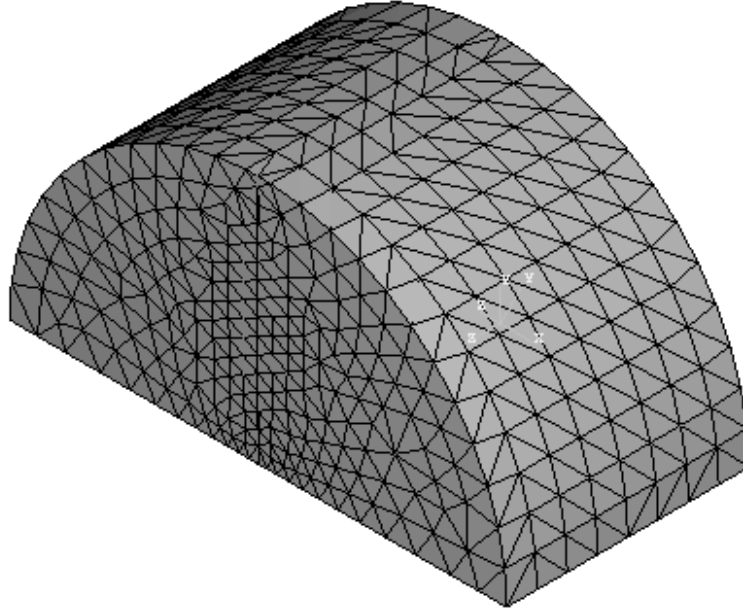
Figure 8: Finite element mesh

faces lying on the notch plane. The notch width b_0 is assumed negligible and
is not visible in the previous figures. The maximum dip vector of the bedding
planes is inclined $45°$ respect to the borehole axis and lies in the plane of the
notch. Figure 8 shows the finite element mesh as generated by the commercial
code ABAQUS. It consists of type-C3D4 four-nodes three-dimensional elements.
A rigid displacement downward is applied to the upper part of the specimen, as
shown in Figure 6.

$f_{t\|s}$	$G_{f\|s}$	$w_{m\|s}$
MPa	N/m	mm
2	38	0.1

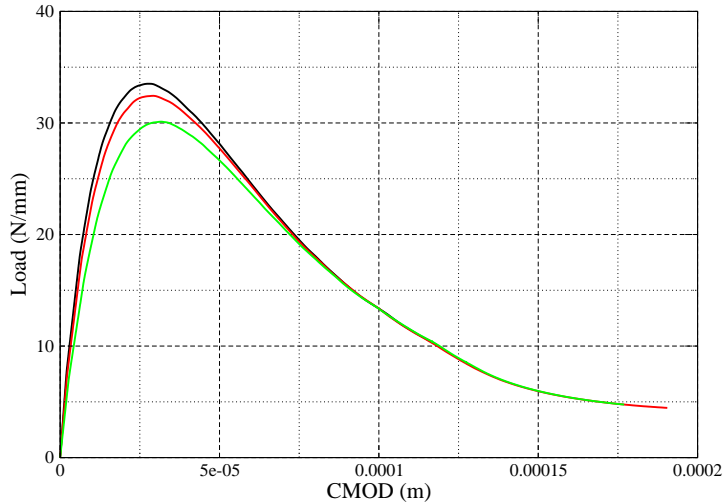Table 5: Fracture properties of planes normal to the bedding.

Figure 9: Load per unit specimen thickness vs Crack Mouth Opening Displacement plot per unit specimen thickness; upper curve a_0=5.4 mm, middle curve a_0=6.0 mm, lower curve a_0=7.3 mm

6. Numerical results

The NLFM model described above was utilized to assess first the combination of parameters giving the numerical response that fits better the experimental observations. These parameters are $G_{f\|s}$, $f_{t\|s}$ and $w_{m\|s}$. However, after fixing α in the softening law of Eq.11, only two of three parameters are independent. In the numerical tests, a reference value for $f_{t\|s}$ was assumed equal to 2 MPa, that is recommended by Bock [21]. The baseline values for parameters are reported in Table 5. The corresponding P-CMOD curves comprises of the experimental results of Figure 3 is presented in Figure 13).

The sensitivity of the response to the parameters was evaluated by performing four model runs by combining perturbations of +-25% to $f_{t\|s}$ and $w_{m\|s}$. Figure 10 shows the results for $a_0 = 6$ mm.

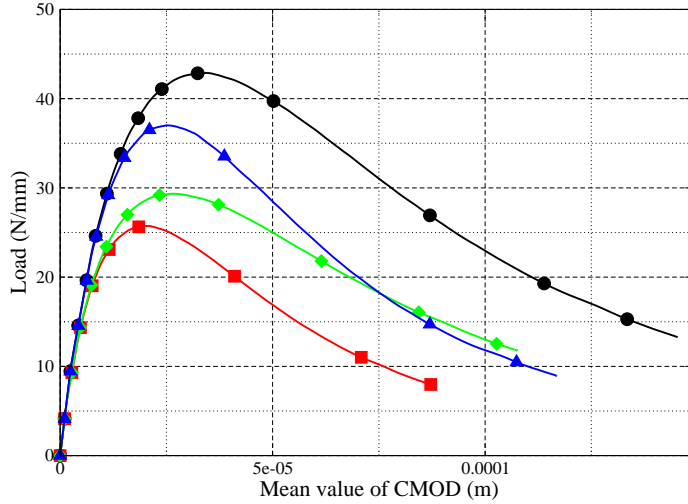In order to evaluate the sensitivity of the response to notch depth a_0, three

Figure 10: Sensitivity of load vs CMOD diagram on f_t and w_m (a_0=6 mm); (a) a circle indicates both parameters increased of 25%; (b) a triangle indicates f_t increased and w_m decreased; (c) a rhombus indicates f_t decreased and w_m increased; (d) a square indicates both parameters decreased of 25%;

models (diameter D=80 mm, thickness s=39 mm, support distance L=62 mm) were set up accordingly to minimum (5.3 mm), most probable (6 mm) and maximum (7.3 mm) values of a_0 values of the selected specimens by using the parameters of Table 5. Figure 9 shows the vertical load per unit specimen thickness P/S plotted against CMOD for all cases.

It is worth noting that, given the anisotropy, CMOD is not uniform along the specimen thickness. Figure 14 represents the applied load P plotted against CMOD evaluated at the extremities of the notch, while Figure 13 represents CMOD evaluated at the specimen center, conforming to the experimental setup.

Due to the negligible value of the tangential stress acting on the coordinate planes, the normal stress on the bedding plane σ_{ns} can be assumed as the mean value between σ_{yy} and σ_{zz} (tractions are assumed as positive). Figure 11 shows
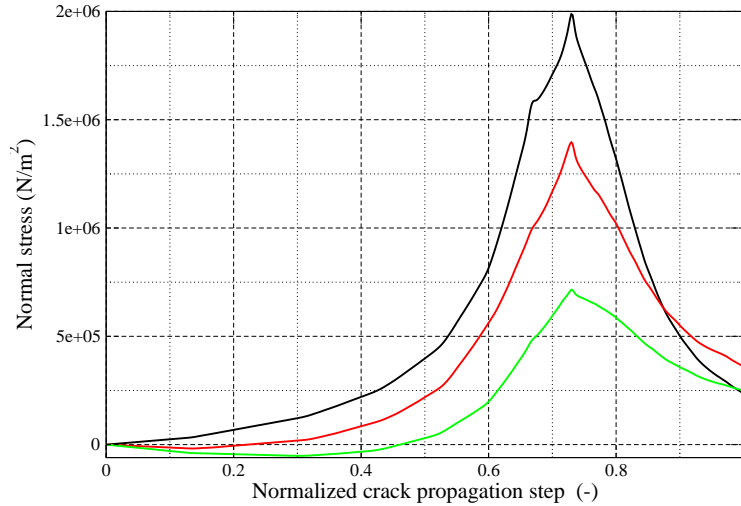
19

Figure 11: Normal stress at a fixed location ($x = 0$, $y = 0.022$ m, $z = 0.02$ m) for notch depth 7.3 mm; upper curve σ_x, curve in the middle σ_y, lower curve σ_z

that $\sigma_{n\mathrm{s}}$ is larger than 1 MPa (estimate of $f_{\mathrm{t}\perp\mathrm{s}}$ from Bock [21]), therefore a second damage mechanism can be activated. The hypothesis that the energy dissipation occurs just on the crack surface along the notch should be removed. In order to characterize the energy dissipated on the volume of OPA around the crack tip, a more complex crack growth mechanism should be considered.

As previously mentioned, the use of K_{Ic} for OPA is misleading because K_{Ic} depends on specimen size. To demonstrate this assertion, a numerical investigation on the effect of size-scale is given in what follows. It is physically difficult to increase the specimen size while keeping constant all the geometrical ratios. Instead, in the context of a numerical analysis, this operation is relatively easy. In fact, the crack model includes an intrinsic length, which is assumed as a material constant, independent on the specimen size. Thus, the finite element mesh around the fictitious crack tip can be kept constant whereas the model size grows. This condition is applied to the models used to obtain P-CMOD curves
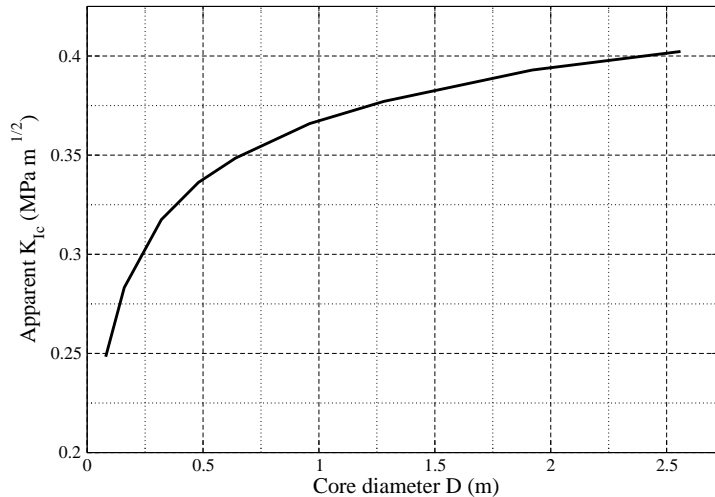
20

Figure 12: Apparent K_{Ic} as a function of specimen size

of Figure 13 and 14 (core diameter $D = 80$ mm and 160 mm, respectively).

It was observed that CPU time grows quickly with size. Therefore, in order to enlarge the size range up to 2560 mm for D, the initial value of thickness (6 mm) was kept for all the simulations. Especially for largest D values, this action would cause large out-of-plane displacements u_3 along z. These displacements would not occur if the thickness were scaled with size, therefore, the boundary condition $u_3 = 0$ was applied along the intersection curve between the external specimen surface and plane $z = 0$.

Due to the anisotropic behavior, a small reduction of the peak load is experienced under this condition. For example, in the case of D equal to 80 mm and $a_0=6$ mm, the peak load in Figure 9 is 32.43 N/mm while the corresponding peak load, utilized in Eq. 10 to obtain K_{Ic} in Figure 12 is 31.38 N/mm. Similarly, for $D=160$ mm ($a_0=12$ mm) the peak load in Figure 14 is 55.91 N/mm and the corresponding peak load for K_{Ic} is 50.61 N/mm.

The non-linear process is carried out by using the Newton-Raphson method.
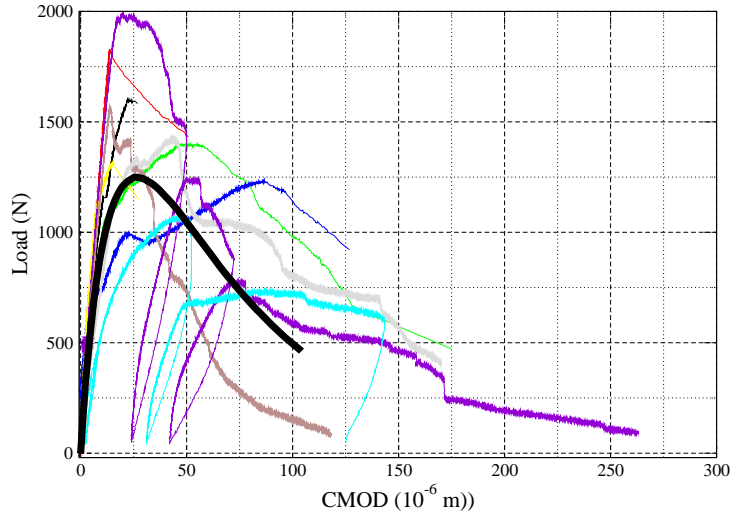
21

Figure 13: Load vs CMOD plot, core diameter D=80 mm (black line) superposed to the experimental results

Since this is an evolutionary quasi-static analysis, the unit of conventional (fictitious) time is assumed as the time necessary to obtain $u_2/D = 0.06/80$ at loading points.

In order to limit the maximum value of out-of-balance nodal forces, time increment is automatically reduced during the analysis. As expected when the CCM is used, lack of convergence increases with size. With reference to $D = 0.08$ m, a mean value of conventional time increment equal to 0.0076 was enough to obtain a maximum out-of-balance nodal force equal to 0.0017 N. With reference to D=2.56 m, it was necessary to reduce the mean value of time increment to 5×10^{-4}, in order to obtain a maximum out-of-balance nodal force equal to 0.0041 N.
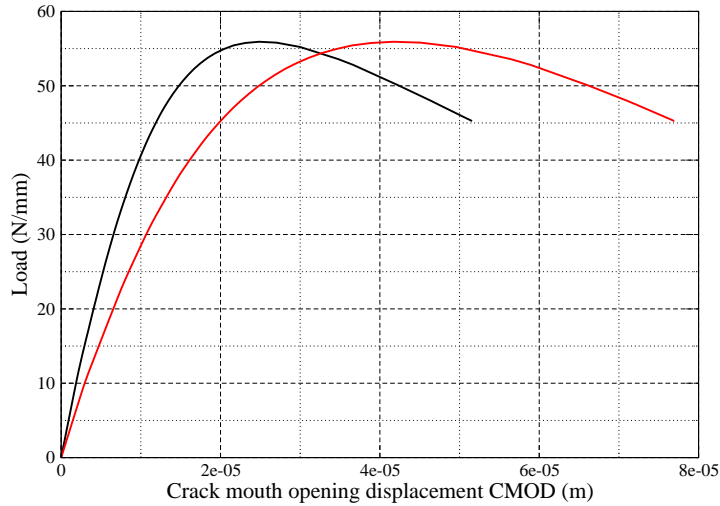
22

Figure 14: Maximum and minimum value of CMOD for 160 mm core diameter

7. Conclusion

In this report the results of an experimental campaign on Opalinus Clay FM parameters are illustrated. By means of a numerical model the FM parameters for cracks normal to the bedding were inferred in the context of NLFM. The number of performed tests is still not sufficient for a complete characterization of OPA, therefore described results and related interpretation must be considered preliminary. However some conclusion can follow.

As discussed previously, the theory of elasticity predicts an infinite stress at the notch tip. Therefore the damage starts to grow at this location, independently on the random distribution of defects. This is the reason why the use of a notch leads to a reduction of the scatter in the experimental peak loads. Dealing with an anisotropic material and initiating the crack perpendicularly to the bedding plane, the benefits in using a notch are effective only in relation to the first damage mechanism, when the crack grows in the notch plane. However,

23

as long as the fracture process zone extends, the benefits are minimized. In fact a large number of bedding planes are candidate to host a second damage mechanism, therefore the random distribution of defects returns to play a central role. As a consequence a large scatter of the peak load shows consequently.

In view of a more detailed understanding of the crack growth occurring in Opalinus Clay and argillites, it is worthwhile to further investigate, through statistical consistent tools, the two damage mechanisms that may occur at the different scales: failure along planes normal to the bedding and failure along the bedding planes. The interaction between the two mechanisms can give rise to peculiar arrangement of the excavation-induced fractures. Given the scatter that is presumable to experience with further tests, it is recommended to utilize the SCB test method. The reason is twofold:

- in a SCB the crack is relatively forced to follow the plane of the notch, whereas in a conventional beam test for example the crack can easily originate also from other points as a consequence of the mineralogical heterogeneity, typical of these geomaterials;

- given the same amount of material the number of tests that can be performed is larger than in other tests, and a more robust statistics about the FM parameters can be obtained.

Consideration of heterogeneities as related to the frequency of layers of different mineralogical content would assist in the interpretation of the results. Another issue that can be addressed is the dependence of FM response on loading rate. Anyway, it is worthwhile to mention that the equipment that is available at IGAG-CNR allows applying load at very slow rate, thus not biased by the occurrence of a pore pressure excess. Finally, as evident from Eq. 9 for fracture toughness, the direction of propagation may depend on both the directional strength and elastic coefficients. In view of a micromechanical model of EDZ a criterion for OPA similar to Eq. 9 should be identified.

8. Acknowledgements

References

[1] S. Yong, K. Evans, C. Fidelibus, and S. Löw. Fracture generation (EZ-B Experiment): a review of the Mont Terri Project literature. Technical Report 2004–40, Mont Terri Project, 2004.

[2] C. Carloni and L. Nobile. Maximum circumferential stress criterion applied to orthotropic materials. *Fatigue Fract. Engng. Mater. Struct.*, 28:825–833, 2005.

[3] G. C. Sih, P. C. Paris, and G. R. Irwin. On cracks in rectilinearly anisotropic bodies. *Int. J. Fracture Mech.*, 1:189–203, 1965.

[4] E. M. Wu. Fracture mechanics of anisotropic plates. In S. W. Tsai, J. C. Halpin, and N. J. Pageno, editors, *Composite Materials Workshop*, pages 20–43, Stamford, CT, 1968. Technomic Press.

[5] V. E. Saouma, M. L. Ayari, and D. A. Leavell. Mixed mode crack propagation in homogeneous anisotropic solids. *Engineering Fracture Mechanics*, 27(2):171–184, 1987.

[6] G. I. Barenblatt. The formation of equilibrium cracks during brittle fracture: general ideas and hypotheses. *Journal of Applied Mathematics and Mechanics*, pages 622–636, 1959.

[7] D. S. Dugdale. Yielding of steel sheets containing slits. *Journal of Mechanics and Physics of Solids*, 8:100–114, 1960.

[8] A. Hilleborg, M. Modéer, and P. E. Petersson. Analysis of crack formation and crack growth in concrete by means of fracture mechanics and finite elements. *Cement and Concrete Research*, 6:773–782, 1976.

[9] P. Bocca, A. Carpinteri, and S. Valente. Fracture mechanics of brick masonry. size effects and snap-back analysis. *Materials and Structures*, 22(131):364–373, 1989. ISSN: 1359-5997.

[10] P. Bocca, A. Carpinteri, and S. Valente. Size effects in the mixed mode crack propagation: softening and snap-back analysis. *Engineering Fracture Mechanics*, 35:159–170, 1990.

[11] P. Bocca, A. Carpinteri, and S. Valente. Mixed-mode fracture of concrete. *International Journal of Solids and Structures*, 27:1139–1153, 1991.

[12] P. Bocca and A. Carpinteri. Snap-back fracture instability in rock specimens: experimental detection through a negative impulse. *Engineering Fracture Mechanics*, 35:241–250, 1990.

[13] F. Barpi and S. Valente. The cohesive frictional crack model applied to the analysis of the dam-foundation joint. *Engineering Fracture Mechanics*, pages 2182–2191, 2010.

[14] B. N. Whittaker, R. N. Singh, and G. Sun. *Rock fracture mechanics: principles, design, and applications*. Elsevier, Amsterdam; New York, 1992.

[15] K. P. Chong, M. D. Kuruppu, and J. S. Kuszmaul. Fracture toughness determination of rocks with core-based specimens. In *Proceedings of FEM-RILEM International Conference of Concrete and Rock*, pages 9–15, Houston, Texas, 1987.

[16] F. Rummel, T. Hettkamp, and U. Weber. Gasfrac self-healing experiment - rock mechanical laboratory tests on Opalinus Clay core samples. Technical Report 98–18, Mont Terri Project, 1998.

[17] F. Ouchterlony. A review of fracture toughness testing of rock. *Solid Mechanics Archives*, 7:131–211, 1982.

[18] C. M. Haberfield and W. Johnston. Determination of the fracture toughness of a saturated soft rock. *Can. Geotech. J.*, 27:276–284, 1990.

[19] Dassault System Simulia Corp., Providence, RI. *ABAQUS, release 6.10*, 2010.

[20] H.A.W. Cornelissen, D.A. Hordijk, and H.W. Reinhardt. Experimental determination of crack softening characteristics of normal and lightweight concrete. *Heron*, 31:45–56, 1986.

[21] H. Bock. RA experiments rock mechanics analyses and synthesis: data report on rock mechanics. Technical Report 2000–02, Mont Terri Project, 2001.